



Surface heterojunction between (001) and (101) facets of ultrafine anatase TiO₂ nanocrystals for highly efficient photoreduction CO₂ to CH₄

Yuhui Cao^a, Qiuye Li^{a,b,*}, Chen Li^a, Junli Li^a, Jianjun Yang^{a,b,*}

^a National & Local Joint Engineering Research Center for Applied Technology of Hybrid Nanomaterials, Henan University, Kaifeng 475004, PR China

^b Collaborative Innovation Center of Nano Functional Materials and Applications of Henan Province, Henan University, Kaifeng 475004, PR China

ARTICLE INFO

Article history:

Received 11 April 2016

Received in revised form 24 May 2016

Accepted 28 May 2016

Available online 30 May 2016

Keywords:

TiO₂

(001) Facets

(101) Facets

Surface heterojunction

CO₂ photoreduction

ABSTRACT

Shape-dependent ultrafine anatase TiO₂ nanocrystals coexposed with (001) and (101) facets are synthesized in isopropanol by the simple solvothermal strategy. Nanotube titanic acid (NTA) was used as the Ti precursor, and hydrofluoric acid was the shape-control reagent. The nanotubular structure of NTA facilitated HF to adsorb on/into NTA, and made the shape-controlled process to be more economical and easier. The ratio of (001) facets of the obtained decahedral TiO₂ nanocrystals can be adjusted from 5 to 51%, and the mean diameter of nanoparticles is about 10–30 nm. The samples are characterized by X-ray diffraction, transmission electron microscopy, X-ray photoelectron spectroscopy, ultraviolet-visible diffuse reflectance spectrum, N₂ adsorption-desorption isotherms, fluorescence and Raman spectroscopy. The truncated octahedral bipyramid TiO₂ nanocrystals with 51% (001) and 49% (101) facets exposing showed the highest photoactivity for CO₂ reduction to CH₄. This remarkable photocatalytic efficiency is attributed to the surface heterojunction between (001) and (101) crystal facets, the small size and large surface area of the truncated octahedral bipyramid TiO₂ nanocrystals.

© 2016 Elsevier B.V. All rights reserved.

1. Introduction

Worldwide energy shortage and global warming have become significant global issues in the view of sustainable development. Photocatalytic reduction of CO₂ on the semiconductor materials is particularly interesting because it is a promising “green chemistry” way for the direct conversion of CO₂ to value-added fuels (CH₃OH, CO, CH₄, etc.) by sunlight [1–5]. CO₂ molecule is chemically inert and stable with a closed-shell electronic configuration and linear geometry. One-electron reduction of CO₂ requires a highly negative potential ($E^0 = -1.9$ V vs NHE at pH = 7), and the product CO₂ radical is too active to control [6]. However, the efficiency of CO₂ photoreduction is still very low, there are many challenges towards improvements in this field. Catalyst plays a certain critical role in the reaction process. Titanium dioxide (TiO₂) and a variety of other semiconductor photocatalysts (ZnO, GaP, WO₃, CdS, ZnGa₂O₄ and

BiOBr etc.) have been fabricated and employed in assorted manners (separately/mixed/metal-doped forms) for enhancing photocatalytic performances [7–12]. Among them, TiO₂ is the most widely investigated catalysts, because of its environment friendly, nontoxicity, cost inexpensive, corrosion resistant, and long-term stability.

Among the anatase, rutile, and brookite polymorphs of TiO₂, anatase TiO₂ usually showed the highest photoactivity toward converting CO₂ to CH₄, which was due to its conduction band is more negative and showed stronger photoreduction [13]. Meanwhile, the activity of the photocatalysts principally depends on their size, shape, and surface properties. Particularly, some physicochemical properties are connected closely with the surface atomic configuration and the exposure of the specific facets. There are three fundamental low-index facets exposed generally in anatase TiO₂ nanocrystals: (001), (010) and (101) facets, and their average surface energies reported in the literature are 0.90, 0.53 and 0.44 J/m², respectively [14–16]. Higher surface energy of (001) facets is more efficient for dissociative adsorption of reactant molecules compared with (010) and (101) facets, which has the high density of active unsaturated coordination Ti atoms and the presence of enlarged Ti–O–Ti bond angles on the surface [17–19]. Both theoretical calculations and experimental results indicated that TiO₂ possessed with a high percentage of (001) facets if their surfaces are

* Corresponding authors at: National & Local Joint Engineering Research Center for Applied Technology of Hybrid Nanomaterials, Henan University, Kaifeng 475004, PR China.

E-mail addresses: qiuyeli@henu.edu.cn (Q. Li), yangjianjun@henu.edu.cn (J. Yang).

surrounded by F^- [20–26]. Among numerous synthesis procedures, HF-assisted hydrothermal/solvothermal methods are widely used to synthesize TiO_2 with (001) facets. Pioneering work by Yang et al. designed anatase TiO_2 microcrystals with exposed (001) facets up to 47% by the use of HF as a shape-controlling agent [20]. Soon afterwards, Yang and coworkers reported a new solvothermal method using $(CH_3)_2CHOH$ as a synergistic capping agent together with HF to synthesize anatase TiO_2 nanosheets with 64% of the (001) facets [27]. And then the TiO_2 with nearly 100% percentage of (001) facets has been synthesized [28]. But it did not mean the higher (001) facets exposure had the better photocatalytic activity [29]. Tachikawa et al. demonstrated that (001) and (101) facets could gather holes and electrons selectively which depended on the number and distribution of potential trapping sites as well as their electronic energy levels [30]. Yu et al. reported TiO_2 with 58% (001) and 42% (101) exposing had the highest activity for CO_2 photoreduction to CH_4 , because the coexposed (101) and (001) facets of anatase TiO_2 can form a surface heterojunction within single TiO_2 particle [31]. It can be concluded that there is an optimal percentage of exposed (001) and (101) facets in anatase TiO_2 to form surface heterojunctions, which are favourable for the separation of photo-generated carriers and enhanced photocatalytic activity.

Different precursors of TiO_2 also have significant effects on the morphology and constitution of the nanocrystals. For the dissolvable titanium salt including TiF_4 [20,32,33], $Ti(SO_4)_2$ [34], $TiCl_4$ [35], $TiOSO_4$ [36], $Ti(OBu)_4$ [37,38] and $Ti\{OCH(CH_3)_2\}_4$ [39], it is hard to control the crystal growth process, which led to the size of TiO_2 with (001) facets crystals more large. On the other hand, undissolvable precursors such as Ti [40], TiN [41], TiC [42], TiS_2 [43] and TiB_2 [44] powders were discovered to play an important role in remaining some of the unique properties of anatase TiO_2 by mild reaction process. Therefore, investigating a new type of precursors for the controllable preparation of ultrafine crystal anatase TiO_2 which expose suitable ratio (001) facets has become an important topic in this field.

NTA has a layered structure and the interlayer distance is about 0.8 nm, larger than the diameter of fluorine ions. This makes it feasible for NTA to provide channels for quick diffusion of fluorine. NTA is thermally unstable and transformed to a novel anatase TiO_2 with large BET surface areas and high concentration of single-electron-trapped oxygen vacancies (V_O^\cdot) during calcining, accompanied by collapse of tubular morphology [45–47]. F^- is easily adsorbed in and outside surface of the nanotube, which help the (001) facets of TiO_2 exposed during structure reorganization. Herein, we look forward to designing an efficient TiO_2 photocatalyst with suitable (001) facets exposure, small nanoparticle size and little HF acid dosage. Through a solvothermal synthesis, TiO_2 nanocrystals with (001) and (101) facets were obtained using NTA as the precursor, HF as the capping agent, the mean particle diameter is to 10–30 nm, and the TiO_2 nanocrystals showed superior photocatalytic productivity for CO_2 reduction to CH_4 . In addition, when Pt nanoparticles were loaded as the electron trap, the photoactivity can be further enhanced. Meanwhile, the relationship between surface heterojunctions of different facets and their photocatalytic activity was investigated.

2. Experimental

2.1. Preparation of 1D nano-structured titanic acid nanotube (NTA)

NTA were synthesized by the hydrothermal process in a concentrated NaOH aqueous solution, a commercial titania P25 was used as the Ti source [46]. Typically, 3 g of P25 was mixed with 300 mL of 10 M NaOH aqueous solution, and followed by the hydrother-

mal treatment at 120 °C in Teflon-lined autoclave for 24 h. The obtained precipitate was washed with deionized water thoroughly until pH = 7, and followed by a filtration process. Then the resulting product was put into 300 mL hydrochloric acid aqueous solution (pH = 1) and stirring for 8 h. At last, the precipitates were washed with distilled water until no Cl^- was detectable. Then, the product was dried in an oven at 100 °C for overnight.

2.2. Synthesis of anatase TiO_2 with coexposed (001) and (101) facets

In a typical synthesis, 1 g of NTA powders were dispersed into 25 mL of absolute isopropanol and stirred for 30 min, and after that, x mL (x is 0, 0.1, 0.2, 0.5, 1 and 1.5) of HF (40 wt%) was added slowly to the suspension, respectively. Then, the suspension was transferred into 50 mL Teflon-lined autoclave and kept at 200 °C for 24 h. After the solvothermal reaction, the resulting precipitates were collected and washed with ethanol and distilled water for several times. Then, the samples were dried in an oven at 80 °C. The obtained samples were denoted as TiO_2 -0HF, TiO_2 -0.1HF, TiO_2 -0.2HF, TiO_2 -0.5HF, TiO_2 -1HF and TiO_2 -1.5HF, respectively. As a reference, the fluorinated P25 was also prepared by the same process in absolute isopropanol adding 0.2 mL of HF (40 wt%), which was denoted as P25-0.2HF.

2.3. Loading Pt nanoparticles as the cocatalyst

For further improving the photocatalytic efficiency, 1 wt% Pt nanoparticles were loaded on the surface of as-prepared samples as the cocatalyst by the in-situ photoreduction method. The corresponding products were denoted as Pt- TiO_2 -0HF, Pt- TiO_2 -0.2HF and Pt-P25, respectively.

2.4. Characterization

X-ray diffraction (XRD) patterns were measured on a Bruker Apex II diffractometer (CuK α radiation, 2θ range 20°–80°, step size 0.08°, accelerating voltage 40 kV, applied current 40 mA). Raman measurement was carried out using a Renishaw inVia Raman spectroscopy, the power of the laser was 1%, and the laser excitation was 532 nm, wavenumber range (100–800 cm^{-1}), and the exposure time was 1 s. The surface area, pore size, and pore volume of the samples were analyzed by nitrogen adsorption at 77 K with the Brunauer–Emmett–Teller (BET) method (Micromeritics, ASAP 2020). Transmission electron microscopic (TEM) images were taken on a JEM-2010 electron microscope at 200 kV. X-ray photoelectron spectroscopy (XPS) measurements were investigated on a Thermo ESCALAB 250Xi with Al K α emission at 1486.6 eV, and all of the binding energies were calibrated by C 1 s at 284.8 eV. UV–visible diffuse reflectance spectra (UV–vis DRS) were obtained on a Shimadzu U-3010 spectrometer, using $BaSO_4$ as a reference. The electron spin resonance (ESR) signals of the samples were tested on a JES FA200 spectrometer at room temperature. The photoluminescence (PL) spectra were recorded on a F-7000 FL spectrophotometer by a typical benchtop fluorimeter (equipped with a 150 W Xe lamp source, using an excited wavelength of 315 nm).

2.5. Photoelectrochemical and photocatalytic activity tests

Photoelectrochemical measurements were conducted in a conventional three-electrode system with 1 M Na_2SO_3 electrolyte on the electrochemical workstation (IM6eX Instruments, ZAHNER, German). The suspension with the obtained sample (0.02 g) and ethanol (0.5 mL) was coated onto a 1 cm \times 1.1 cm fluorine-tin oxide (FTO) glass as the working electrode, a Pt mesh and an Ag/AgCl

electrode (SCE) acting as the counter electrode and reference electrode, respectively. Electrochemical impedance spectroscopy (EIS) experiments were conducted at the bias of 0.4 V and a 250 W Hg lamp was employed as photon source.

Photocatalytic activity was conducted in a closed reactor with the inner capacity of 200 mL containing 125 mL 0.1 M KHCO_3 solution. 0.1 g catalyst was put into the reactor and then ultrasonic to disperse evenly. The ultrapure gaseous CO_2 was flowed through the solution under stirring for 1 h, until it achieved saturated state. The photocatalytic reaction was typically performed at room temperature for 6 h using a high pressure Hg lamp (250 W). The outputs were analyzed by a gas chromatography (GC 9790, Zhejiang, China).

3. Results and discussion

3.1. Catalyst characterization

The crystal structures of the prepared materials were confirmed by XRD and Raman spectroscopy. Fig. 1a shows the XRD plots of all samples. The peaks at 25.25, 37.72, 48.03, 53.91, and 54.99° can be assigned to (101), (004), (200), (105), and (211) crystal planes of anatase TiO_2 (JCPDS 21-1272), respectively [30]. Anatase is the unique phase in all samples except for P25-0.2HF which shows the presence of anatase and rutile. Apparently, the (004) diffraction peak of TiO_2 -0.2HF becomes broader, which indicates massive appearance of (001) facets [21]. Typical anatase phase is revealed from the appearing peaks at about 144 (E_g), 394 (B_{1g}), 514 (A_{1g}), and 636 cm^{-1} (E_g) in Fig. 1b. We can easily observe that the E_g peaks (144 cm^{-1}) of TiO_2 -0.2HF is the lowest. It has been known that E_g and B_{1g} peaks is mainly caused by symmetric stretching vibration and bending vibration of O–Ti–O, while A_{1g} peak is caused by anti-symmetric bending vibration of O–Ti–O [48]. The vibration models of anatase TiO_2 (101) and (001) facets were different with that of no (001) facets exposed, and the intensity of the symmetric stretching vibration modes of O–Ti–O becomes weak when the (001) facets exist [49]. In a word, the higher the percentage of (001) facets, the weaker the intensity of the symmetric stretching vibration modes of O–Ti–O will be, and correspondingly, the intensity of the E_g peaks in the Raman spectra decreased. The information provided from Raman spectroscopy is in agreement with the above XRD results, and the enlarged XRD patterns and Raman spectra are shown in Fig. S1.

The XPS analysis in Fig. 2 gives the surface composition and chemical status of TiO_2 -0.2HF. Four XPS plots of Ti2p, O1s, F1s, and Pt4f are presented. The binding energy of Ti2p_{3/2} and Ti2p_{1/2} (Fig. 2a) is located at 458.4 and 464.1 eV [44], indicating the oxidation state of the Ti element is the same as that of bulk TiO_2 . The O1s peaks consisted of a dominant peak at 529.5 eV and another higher energy peak at 531.9 eV, which can be indexed to Ti–O bonding and surface O–H bonding of TiO_2 -0.2HF, respectively (Fig. 2b) [44,50]. Simultaneously, the existence of F is detected, and the F 1s peak at the binding energy of 684.1 eV in Fig. 2c is a typical value for Ti–F species on the TiO_2 surface [17]. The existence of fluorine would affect the properties of catalyst, and the role of F for the photoactivity will be discussed in the following section. The binding energy peak of Pt 4f_{7/2} and 4f_{5/2} can be observed at 71.4 and 74.9 eV in Fig. 2d, which are in accordance with the standard position of Pt⁰ [40], and indicating Pt⁰ nanoparticles were successfully loaded on TiO_2 -0.2HF surfaces by photo-deposition method.

The morphology and microstructure of the products were shown in Fig. 3. As can be seen from Fig. 3a, TiO_2 -0.2HF nanocrystals are consisted of highly dispersed truncated octahedral bipyramid nanoparticles. The mean particle size is calculated to be 10–18 nm with more than 100 nanoparticles from TEM images (Fig. S2). The HRTEM image (Fig. 3b) shows that the lattice spacing parallel to

Table 1

Effect of different volume of HF on the structural of TiO_2 nanocrystals.

Sample	ACS (nm)	S_{BET} (m^2/g)	Vp (cm^3/g)	APS (nm)	Percentage of (001)
TiO_2 -0HF	12	92	0.6	1.3	5%
TiO_2 -0.1HF	14	91	0.4	7.8	42%
TiO_2 -0.2HF	15	90	0.38	8.6	51%
TiO_2 -0.5HF	18	85	0.27	6.3	36%
TiO_2 -1HF	20	83	0.24	5.8	25%
TiO_2 -1.5HF	30	53	0.3	1.1	8%
P25	25	55	0.51	1.9	–
P25-0.2HF	25	54	0.5	1.8	–

ACS—average crystallite size; S_{BET} —BET surface area; Vp—pore volume; APS—average pore size.

the top and bottom facets is ca. 0.235 nm, which corresponds to the (001) planes of anatase TiO_2 . Another set of lattice fringes with the spacing of 0.351 nm corresponding with the (101) planes was also clearly revealed from the picture. And the crystal orientation of (101) and (001) faces with an interfacial angle of 68.3°, which indicates the top and bottom facets of the truncated octahedral bipyramid TiO_2 are the (001) facets, the lateral isosceles trapezoid corresponds to (101) facet [20]. On the basis of the above truncated octahedral bipyramid structural information, the percentage of the (001) facets in TiO_2 -0.2HF was estimated to be 51% as calculated by a reported method [51]. As can be seen in Fig. 3c and d of TiO_2 -0HF catalyst, the octahedral bipyramid TiO_2 -0HF nanocrystals exposing with a great deal of (101) facets, and the average particle size is 11–17 nm (Fig. S2). The information further confirms the contribution of F[–] to the exposure of (001) facets. TEM images of TiO_2 -xHF (x is 0.1, 0.5, 1 and 1.5) are shown in Fig. S3. The dimension of the TiO_2 nanocrystal grew up apparently with the augment of HF. The nanoparticles aggregated seriously to about 30 nm and the proportion of (001) facets decreased to 8% when 1.5 mL was added to the reaction. The amount of HF has a large effect on the morphology and size of the TiO_2 nanocrystals, and the detailed information was listed in the following Table 1.

Pt often plays a crucial role for the improvement of the photoactivity, especially for the deep reduction of CO_2 to CH_4 in the photoreduction of CO_2 . Fig. 3e and f showed that Pt⁰ nanoparticles were uniformly deposited on the TiO_2 -0.2HF surfaces and the average particle size was 1–2 nm. Highly dispersed Pt⁰ nanoparticles are beneficial for the accumulation of electrons, which can promote the separation of electrons and holes, and then further enhance the reduction of CO_2 ; while Pt⁰ on the TiO_2 -0HF surfaces aggregates to 4–6 nm as shown in Fig. 3g and h. It is conventional understanding that (101) facets should have more strongly reductive electrons because their bottom of CB in the order (101)>(001) [52]. Therefore, (101) facets with a Pt-loading are easier to form Pt aggregates on the surfaces due to their different surface electronic structures and reconstructions during the Pt deposition process.

Fig. 4 displays N_2 adsorption-desorption isotherms and the corresponding pore size distribution curve for the prepared TiO_2 samples. All of the samples exhibited similar type-IV isotherms with an H3 hysteresis loop at a relative pressure range of 0.7–0.95 according to the IUPAC classification, which are typical characters of mesoporous materials [53]. Pore size distribution curve (insert) of the TiO_2 -0.2HF sample, with a peak at 8.6 nm, was achieved through BJH analysis. Quantitative details on BET surface areas, pore volume and average pore size of the TiO_2 samples are presented in Table 1. The BET surface areas of catalysts from NTA precursor are larger than P25 and P25-0.2HF except TiO_2 -1.5HF. With the increasing of HF from 0 to 1 mL, the surface areas of the samples decreased a little sequentially. However, the specific surface areas of TiO_2 -1.5HF (53 m^2/g) apparently decreased about two times than that of TiO_2 -0HF (92 m^2/g), which is caused by plenty of HF, through selectively corroding (001) facets and leading to irreg-

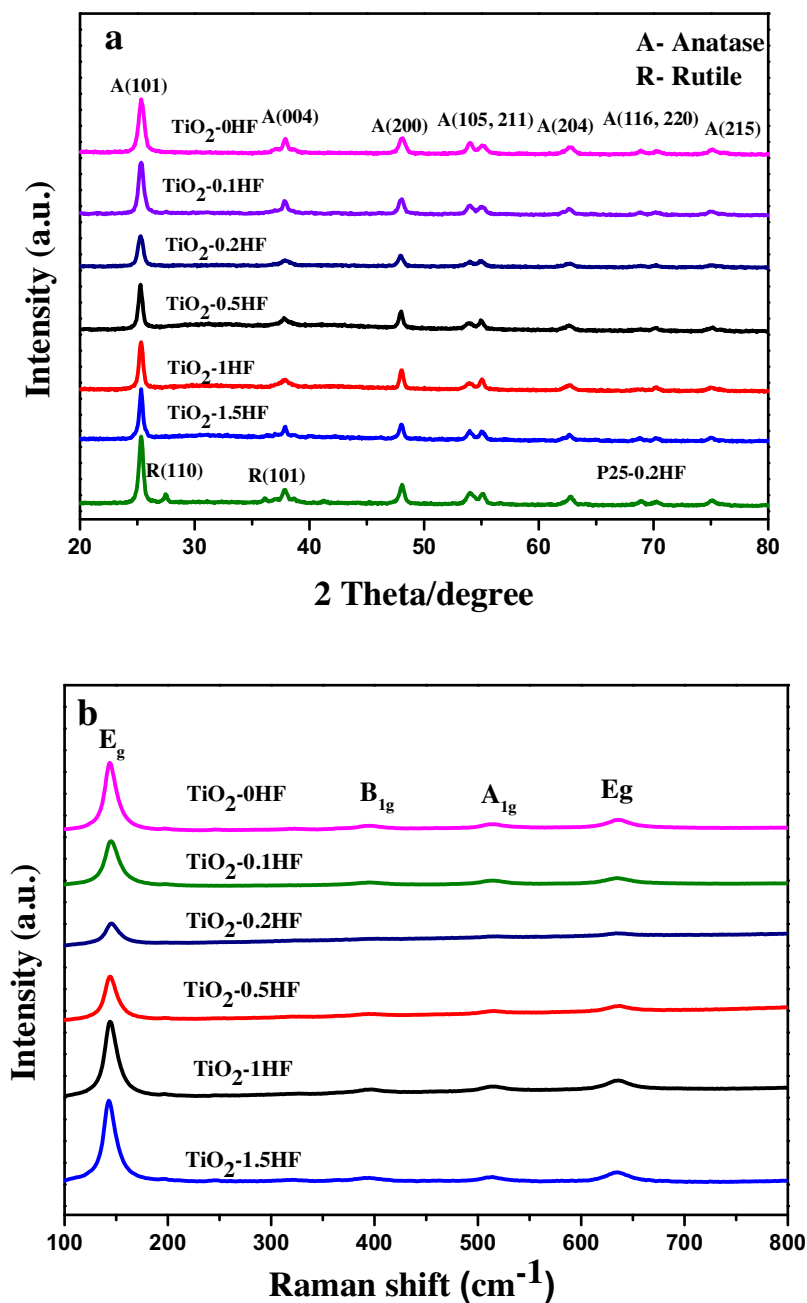


Fig. 1. XRD and Raman patterns of the photocatalysts.

ular growth of TiO₂ nanoparticles (TEM images of TiO₂-1.5HF was shown in Fig. S2). The average pore size of TiO₂-0.2HF is 8.6 nm larger than any other sample, which is beneficial for adsorption of CO₂.

The UV–vis optical absorption spectra obtained by the diffuse reflectance of as-prepared TiO₂ are shown in Fig. 5. The onset of the absorption edge for TiO₂-0HF is at ca. 410 nm, which is consistent with the band gap of anatase TiO₂ (3.02 eV). Compared with TiO₂-0HF, the absorption edge of TiO₂-xHF has not an obvious shift. Surprisingly, absorption intensity of TiO₂-0.2HF is significantly higher than that of other samples, which is due to the exposure of abundant (001) facets. The high density of active unsaturated coordination Ti atoms and the presence of enlarged Ti–O–Ti bond angles on the (001) facets surface, which make the existence of oxygen defects [54]. Based on the analysis above, it can be con-

cluded that the TiO₂-0.2HF might result in the efficient utilization of UV–vis light and exhibit high photocatalytic activities.

3.2. Photocatalytic activity

The CO₂ photoreduction performance of the catalysts was shown in Fig. 6. Both reactions under light without the catalysts and in dark with the catalysts were tested as contrast experiment. A very trace amount of CH₄ or CO was detected in the two comparison tests, indicating that the reaction was indeed a photocatalytic process.

All of the prepared TiO₂ nanocrystals exhibited photocatalytic activity that was significantly better than the commercial P25, because of the anatase phase structure. The conduction band edge potential of anatase TiO₂ is more negative [vs normal hydrogen

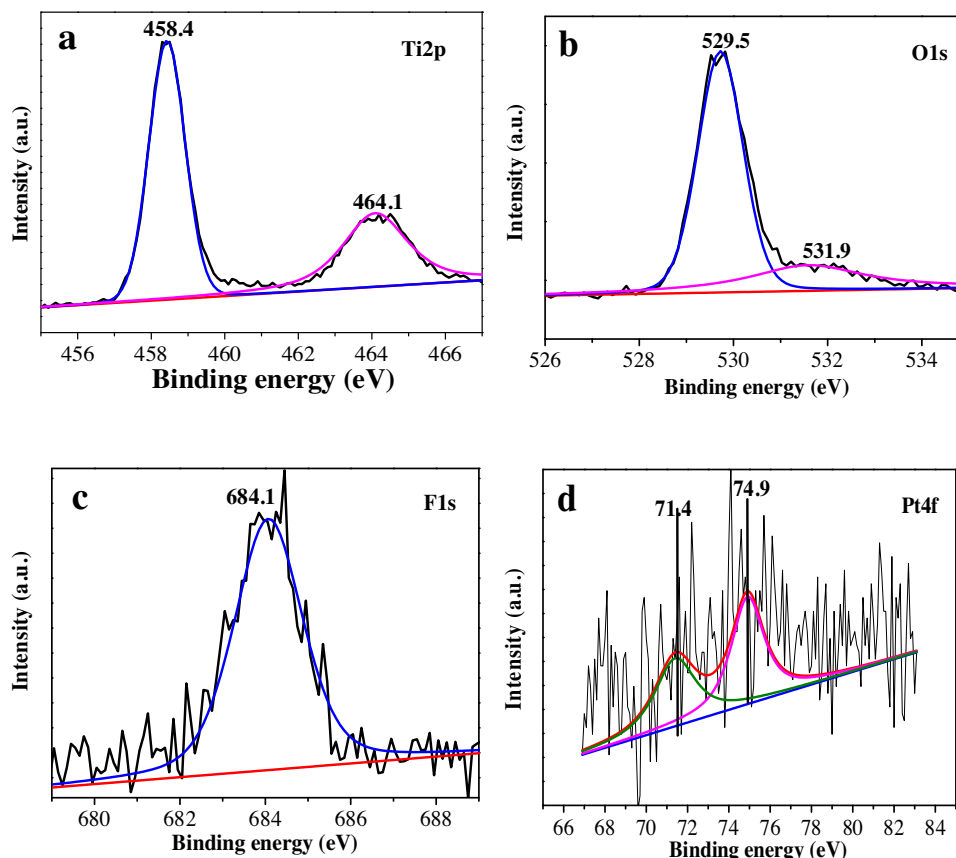


Fig. 2. XPS spectra of Ti2p (a), O1s (b), F1s (c) and Pt4f (d) in Pt-TiO₂-0.2HF sample.

electrode (NHE)] than the CO₂/CH₄ reduction potential, thus, the anatase TiO₂ can efficiently reduce CO₂ into CH₄ under Hg lamp irradiation [13]. Although BET surface area of TiO₂-0HF was higher, the photoreduction CO₂ activity on TiO₂ nanocrystals with exposed (001) facets was much higher than its except TiO₂-1.5HF. This indicated (001) facets played a key role in the enhancement of the photoactivity. The photocatalytic activity of these catalyst samples can be rationalized as TiO₂-0.2HF > TiO₂-0.1HF > TiO₂-0.5HF < TiO₂-1.5HF. Based on the DFT calculations, the (101) and (001) facets of anatase TiO₂ exhibit different band structures and band edge positions [31]. Thus, the coexposed (101) and (001) facets of anatase can form a surface heterojunction within a single TiO₂ particle, which is beneficial for the transfer of photogenerated electrons to (101) and holes to (001) facets, respectively [31]. TiO₂-0.2HF has the highest CH₄ production rate of 1.58 μmol h⁻¹ g⁻¹, which was owing to the optimal ratio of the (001) and (101) facets. However, the inferior photocatalytic activity of TiO₂-1.5HF than TiO₂-0HF was on account of two reasons: one is the smaller specific surface area of the later, and the other is deficiencies appeared on the surface of TiO₂-1.5HF with the corrosion of HF, which enhanced the recombination of photo-generated carriers and reducing the photoactivity. Considering the impact of fluorine on photoactivity of the catalyst, while defluorination may change the morphology and surface state of TiO₂, the catalytic activity of P25-0.2HF was tested under the same conditions, and a slightly higher photocatalytic CH₄ production rate (0.21 μmol h⁻¹ g⁻¹) was obtained than 0.1 μmol h⁻¹ g⁻¹ of P25, which indicated the present of appropriate F on the surface was favourable to enhance CO₂ photoreduction. Surface Ti-F electronegative groups can act as trapping sites for photo-generated electrons and facilitate transfer to surface-adsorbed CO₂ molecules [42]. It is worth mentioning that a novel anatase TiO₂ was obtained

Table 2

CH₄ production rate of TiO₂-0.2HF in different solvent systems.

system	KHCO ₃ (CO ₂)	H ₂ O (CO ₂)	KHCO ₃ (N ₂)
CH ₄ (μmol g ⁻¹ h ⁻¹)	1.58	1.56	0

by dehydration of NTA at elevated temperature which contains high concentration of single-electron-trapped oxygen vacancies (Vo[•]) in our previous study [46,47]. Here we also tested single-electron-trapped oxygen vacancies (Vo[•]) of TiO₂-0HF and TiO₂-0.2HF, as shown in Fig. S4. A large amount of Vo[•] exist in the bulk of TiO₂-0HF, as for TiO₂-0.2HF samples, there exist a little Vo[•]. This predicts the existence of HF can significantly reduce the defect in the bulk phase of the TiO₂ (Vo[•]). Consequently, it helps reduce the probability of electron hole recombination in the compound, and prompt charge carriers participating into the photocatalytic redox reaction. Based on the above discussion, the photocatalytic activity of the TiO₂ samples is strongly affected by many factors, including the optimum ratio of the exposed (001) to (101) facets, and surface area, crystal structure of catalyst and appropriate amount of F. Surface heterojunction between (001) and (101) facets of TiO₂ nanocrystals is one of most important reasons (seen from the following PL and EIS spectra).

To confirm that CH₄ is formed from CO₂, we have compared the rates of CH₄ formation in the presence of H₂O instead of KHCO₃ solution under CO₂ atmospheres, and the formation rate of CH₄ of TiO₂-0.2HF catalyst reached to 1.56 μmol h⁻¹ g⁻¹, which is equivalent to the production rate of CH₄ (1.58 μmol h⁻¹ g⁻¹) in KHCO₃ solution. In addition, when the reactor was filled with N₂ (instead of CO₂) in KHCO₃ solution, no carbon-containing compounds were detected either (Table 2). The results illustrate that the C species in the photocatalytic products of CH₄ comes from CO₂.

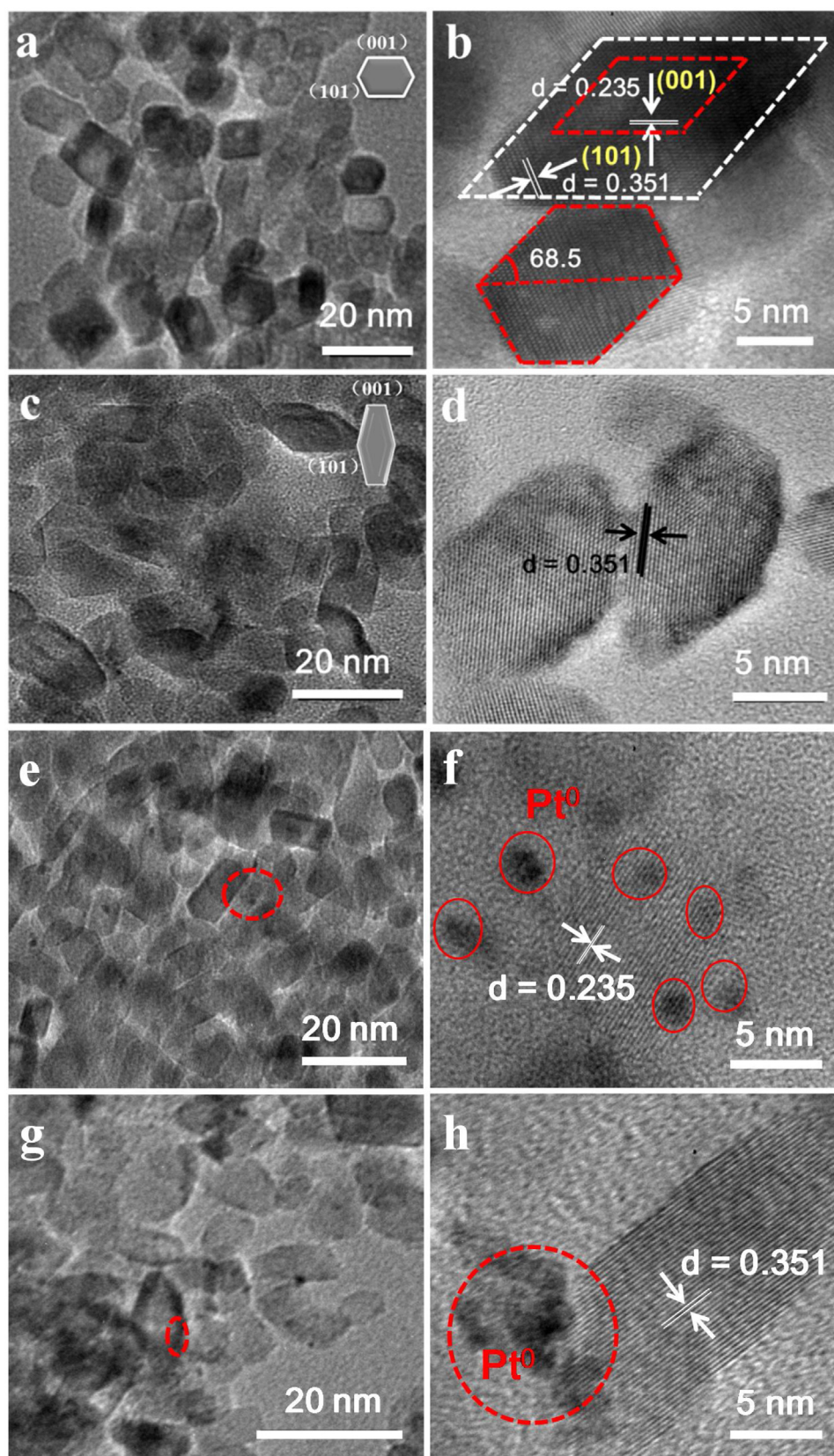


Fig. 3. TEM and HRTEM images of TiO₂-0.2HF (a, b), TiO₂-0HF (c, d), Pt-TiO₂-0.2HF (e, f), Pt-TiO₂-0HF (g, h).

The effect of 1% Pt⁰ in TiO₂ samples on the photoreduction performance of CO₂ was shown in Fig. 7. Obviously, after loading Pt⁰ nanoparticles, the photocatalytic activity increased inordinately.

Pt-TiO₂-0.2HF shows the largest increase of photocatalytic CO₂ reduction activity for CH₄ generation compared with Pt-P25 and Pt-TiO₂-0HF. One of the most important reasons is small size and

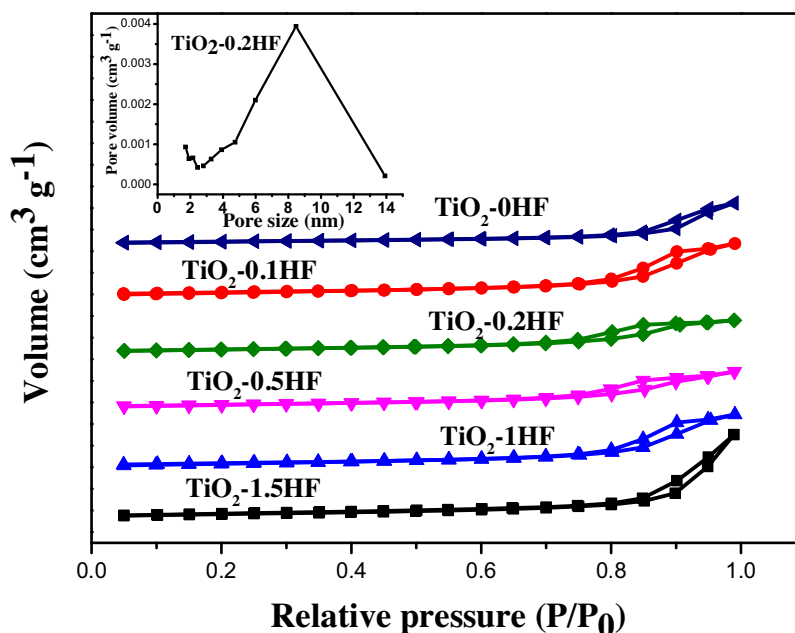


Fig. 4. Nitrogen adsorption–desorption isotherms and pore size distribution curve of TiO_2 -0.2HF displays in inset.

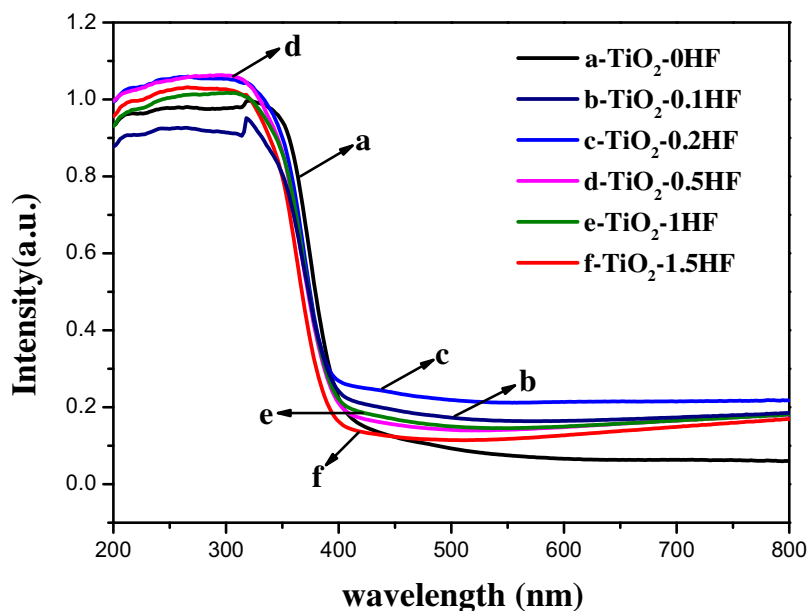


Fig. 5. UV-vis diffuse reflectance spectra of different TiO_2 nanocrystals.

uniformly distributed Pt nanoparticles on the TiO_2 -0.2HF surface, as above mentioned (TEM). The AQE based on CH_4 production over Pt- TiO_2 -0.2HF was calculated to be 0.22% (details displayed in Supporting Information). As shown in inset of Fig. 7, the stability test of Pt- TiO_2 -0.2HF was conducted by cycle reaction, and each cycle was performed for 6 h. After each cycle, CH_4 in the system was degassed by N_2 and then CO_2 was reintroduced into the reactor. The rates of CH_4 formation declined apparently in the second reaction, but it did not show significant change in the subsequent cycles. After four cycles of reaction, the formation rate of CH_4 of Pt- TiO_2 -0.2HF catalyst reached to $3.15 \mu\text{mol h}^{-1} \text{g}^{-1}$. Indeed, there are many factors affecting the photocatalytic activities, for this sample, the decrease of photoactivity was possibly attributed to either the inactivation of some active sites or the structural change

of the catalyst in the reaction process. IR and XPS experiments were carried out to detect surface species of recycled catalysts, but no apparent change was observed (Fig. S5). We believed that the decrease in activity was typically resulted in the TiO_2 nanoparticles aggregated in aqueous solution after a long time. In order to prove our conjecture, the recycled catalyst is characterized by N_2 adsorption-desorption isotherms, the specific surface areas of the recycled catalyst ($75 \text{ m}^2/\text{g}$) decreased apparently compared with that of original catalyst ($90 \text{ m}^2/\text{g}$), and the decreased percentage of the specific surface areas is approximately equal with the decline yield of catalytic activity.

The feasibility of H_2 and O_2 production is investigated with a gas chromatography (GC 7920, Beijing, China) during the process of photoreduction CO_2 . The formation rate of H_2 of Pt- TiO_2 -0.2HF cat-

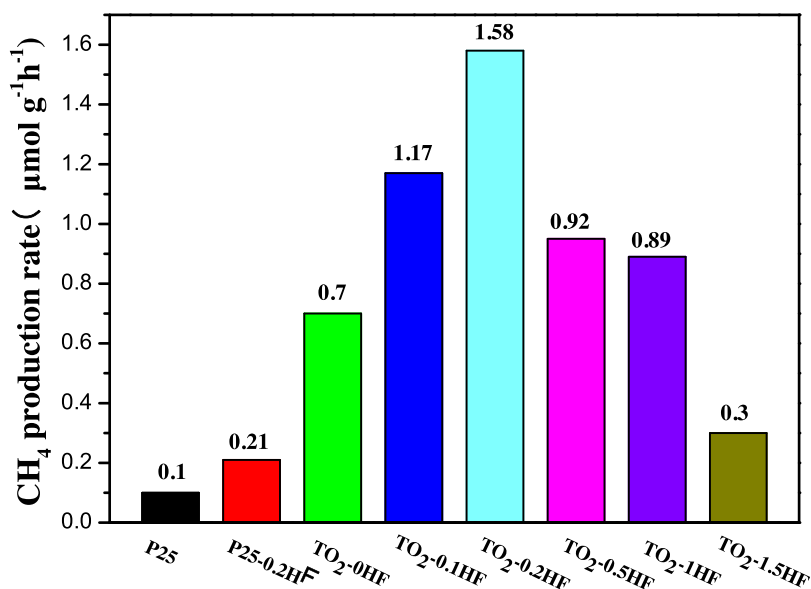


Fig. 6. Photocatalytic activity of CH₄ production rate of P25, P25-0.2HF and TiO₂-xHF samples.

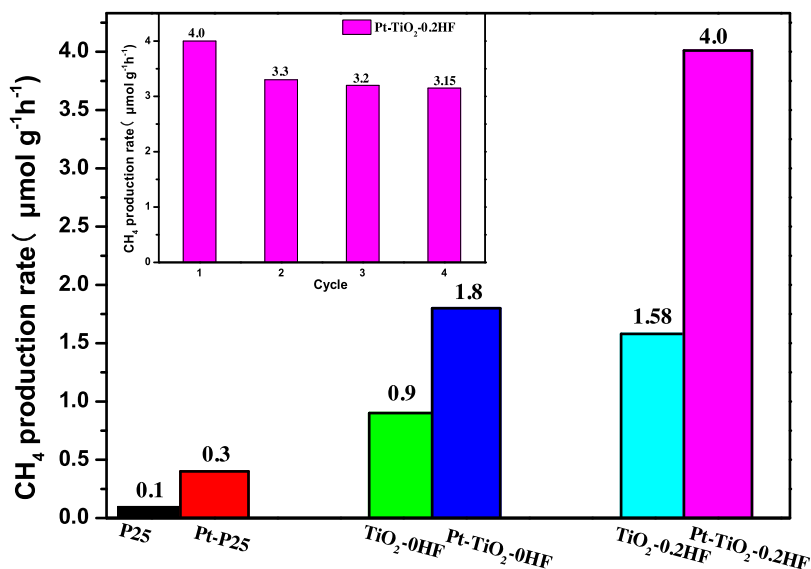


Fig. 7. CH₄ production rate of Pt-P25, TiO₂-0HF and TiO₂-0.2HF samples and the inset displays the stability of Pt-TiO₂-0.2HF nanoparticles on CO₂ photoreduction in the consecutive four cycles.

alyst reached to $0.92 \mu\text{mol h}^{-1} \text{g}^{-1}$, which is significantly inferior to the production rate of CH₄ ($4 \mu\text{mol h}^{-1} \text{g}^{-1}$). Based on the literature results [55,56], we believe the relatively lower yield of H₂ production in this work is possibly due to the following two reasons: (1) protons or $\cdot\text{H}$ radicals formed by the photodissociation of water are competitively consumed by CO₂ reduction intermediates like CO₂⁻ to produce CH₄; (2) the produced H₂ could be consumed by reverse reactions with CO or O₂. The formation rate of O₂ of Pt-TiO₂-0.2HF catalyst reached to $5.2 \mu\text{mol h}^{-1} \text{g}^{-1}$, which is a little higher than the production rate of CH₄ ($4 \mu\text{mol h}^{-1} \text{g}^{-1}$). The production rate of O₂ and CH₄ is not in accordance with the molar ratio, which is possibly caused by the consumption of residual O₂ in the reactor through the reaction with photogenerated electrons: $\text{O}_2 + \text{e}^- \rightarrow \text{O}_2^-$ [57,58], and then O₂⁻ could take consecutive reactions with other intermediate to form traces of oxygenated chemicals such as CH₃OH, HCOOH et al.

To further evaluate the photocatalytic performance in liquid phase, we examined photocatalytic activity of the as-prepared

TiO₂-xHF samples by methylene blue (MB) degradation. As shown in Fig. S6, TiO₂-0.2HF also shows the superior photocatalytic activity and the degradation rate is up to nearly 90% within 10 min under Xe arc lamp irradiation. This also further revealed TiO₂-0.2HF with proper ratio (001) facets has a broad application.

3.3. The mechanism of the photocatalytic reaction

In the photocatalytic reactions, the separation of carriers is one of the effective factors to enhance the photocatalytic reactivity, especially in photoreduction CO₂ reactions. The photoluminescence (PL) emission mainly results from the recombination of excited electrons and holes, which can be considered as an effective approach for understanding the separation capacity of the photo-induced carriers. A low PL intensity also indicates the decrease in recombination rate [59,60]. Fig. 8 shows the fluorescence spectra of the samples in a wavelength range of 350–550 nm. It can be seen that all the peaks displayed similar shapes, and three main

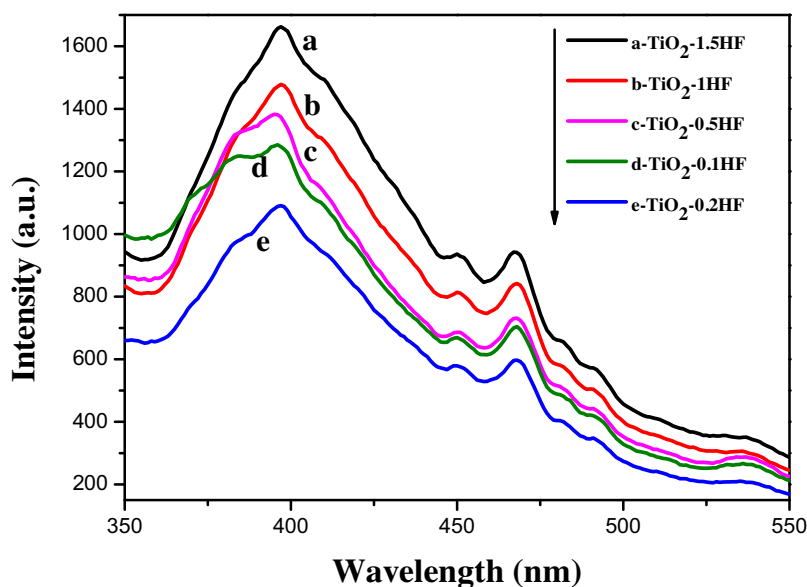


Fig. 8. PL spectra of the TiO_2 -xHF photocatalysts (excited wavelength: 315 nm).

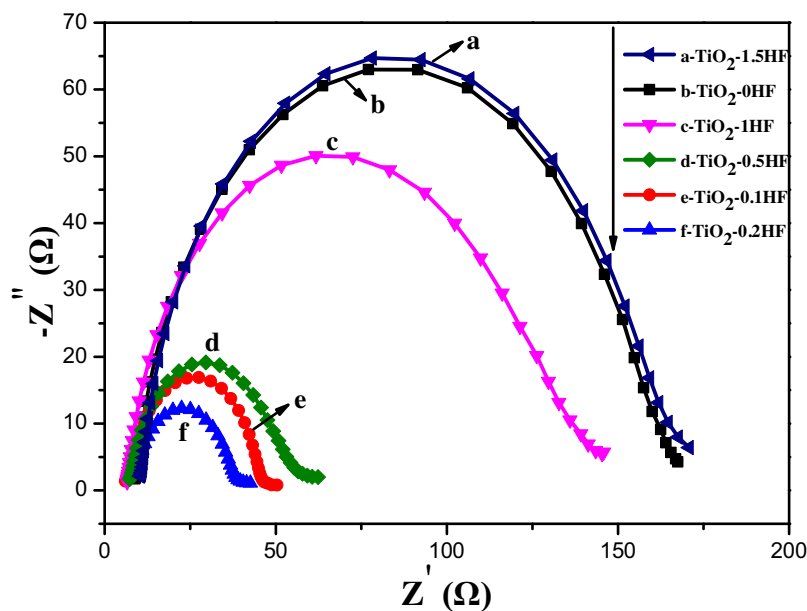


Fig. 9. Nyquist plots of the TiO_2 -xHF samples.

characteristic peaks appeared at 398, 451, and 468 nm, which was corresponding to the energy levels of 3.12, 2.75, and 2.65 eV, respectively. That's to say, fluorescence peaks at 398 attributed to the emission peak towards excitation the band gap of anatase TiO_2 , and the other two fluorescence peaks derived from band-to-band transition of free carriers [61]. The TiO_2 -0.2HF sample has the weakest PL emission probably because of the relatively low electrons and holes recombination rate. PL measurement results are in consistent with the order of the photocatalytic activity.

EIS spectra is often used for characterizing the conductivity of an electrode, a small circular radius usually shows a lower charge transfer resistance [62]. Fig. 9 shows the Nyquist plots of different samples, TiO_2 -1.5HF and TiO_2 -0HF show large semicircles, which is due to the higher percentage of the exposed (101) facets on the TiO_2 sample, which plays the role of recombination centres for photo-generated carriers and thus inhibit the charge separation. The

better activity of TiO_2 -0HF than TiO_2 -1.5HF may be on account of the larger surface area. At the same time, it can obviously be seen that semicircles of TiO_2 -1HF, TiO_2 -0.5HF, TiO_2 -0.1HF modified electrodes decreased, which can be mainly attributed to surface heterojunction between (001) and (101) facets of TiO_2 . Interestingly, the impedance arc radius of TiO_2 -0.2HF is the smallest among samples implying that the highest separation efficiency of photo-generated electron-hole pairs was achieved from TiO_2 -0.2HF. This is attributed to the appropriate proportion between (001) and (101) facets, which extremely prevents the direct recombination of electrons and holes.

The schematic diagram of proposed mechanism of CO_2 photoreduction process is shown in Fig. 10. When the ultrafine applanate truncated octahedral bipyramid TiO_2 nanocrystals was irradiated by Hg lamp, photo-induced electrons and holes were produced. The photogenerated electrons on the (001) facets could transport to the

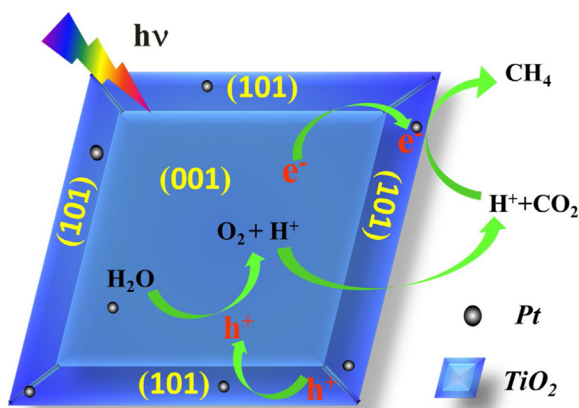


Fig. 10. Schematic diagram of mechanism of photocatalytic process.

(101) facets due to their conduction band offset, and then react with the adsorbed CO_2 to generate CH_4 subsequently. Correspondingly, the photogenerated holes on the (101) facets could transfer to the (001) facets, and then react with the adsorbed H_2O to generate O_2 and H^+ . After loading of Pt nanoparticles, photo-generated electrons can be easily trapped by Pt because of its lower Fermi energy level, improving the separation efficiency of the photo-generated electron-hole pairs, and then the photoreduction rate of CO_2 to CH_4 was accelerated.

4. Conclusions

In brief, ultrafine anatase TiO_2 nanocrystals with controllable coexposed (001) and (101) facets were prepared by a facile solvothermal strategy. 1D NTA transformed to applanate truncated octahedral bipyramid TiO_2 nanocrystals, and the percentage of (001) facets can be adjusted from 5 to 51%. TiO_2 -0.2HF with 51% of (001) facets and 49% (101) facets exhibited the highest photocatalytic activity in terms of both photoreduction CO_2 and photodegradation of MB. PL and EIS spectra results proved that the efficient surface heterojunctions between (001) and (101) facets are favourable for the separation of photogenerated charge carriers. What is more, the smaller size reduces recombination probability of photocarriers in the bulk. The photoreduction rate of CO_2 to CH_4 reached to $1.58 \mu\text{mol h}^{-1} \text{g}^{-1}$ on TiO_2 -0.2HF, and the photoactivity increased remarkably to $4.0 \mu\text{mol h}^{-1} \text{g}^{-1}$ after loaded Pt nanoparticles. In addition, the efficiency could remain nearly 80% after four cycle reactions, indicating the catalyst has a long-term stability. Moreover, little HF dosage is beneficial for subsequent industrial production, and this kind of ultrafine TiO_2 nanocrystals with surface heterojunction is potential for the development of solar cells, optoelectronic devices, sensors and heterogeneous catalysts.

Author contributions

The manuscript was written through contributions of all authors. Yuhui Cao carried out the total experiment and wrote the first manuscript. Chen Li and Junli Li participated in the data analysis. Qiuye Li supervised the project. Jianjun Yang provided the facilities and discussions related to them. All authors read and approved the final manuscript.

Acknowledgments

The authors gratefully acknowledge the support of the National Natural Science Foundation of China (Nos. 21103042 and 21471047), Program for Science & Technology Innovation Talents

(15HASTIT043) and Innovative Research Team (16IRTSTHN015) from the University of Henan Province, and Program for Changjiang Scholars and Innovative Research Team in University from the Ministry of Education of China (PCS IRT1126).

Appendix A. Supplementary data

Supplementary data associated with this article can be found, in the online version, at <http://dx.doi.org/10.1016/j.apcatb.2016.05.071>.

References

- [1] S.C. Roy, O.K. Varghese, M. Paulose, C.A. Grimes, *ACS Nano* 4 (2010) 1259–1278.
- [2] J. Lee, D.C. Sorescu, X. Deng, *J. Am. Chem. Soc.* 133 (2011) 10066–10069.
- [3] D. Mei, X. Zhu, C. Wu, B. Ashford, P.T. Williams, X. Tu, *Appl. Catal. B Environ.* 182 (2016) 525–532.
- [4] S.N. Habisreutinger, L. Schmidt-Mende, J.K. Stolarczyk, *Angew. Chem. Int. Ed.* 52 (2013) 7372–7408.
- [5] J.L. White, M.F. Baruch, J.E. Pander III, Y. Hu, I.C. Fortmeyer, J.E. Park, T. Zhang, K. Liao, J. Gu, Y. Yan, T.W. Shaw, E. Abelev, A.B. Bocarsly, *Chem. Rev.* 115 (2015) 12888–12935.
- [6] D. Chen, X. Zhang, A.F. Lee, *J. Mater. Chem. A* 3 (2015) 14487–14517.
- [7] X. Dong, F. Li, N. Zhao, F. Xiao, J. Wang, Y. Tan, *Appl. Catal. B Environ.* 191 (2016) 8–17.
- [8] X. Chen, Y. Zhou, Q. Liu, Z. Li, J. Liu, Z. Zou, *ACS Appl. Mater. Interfaces* 4 (2012) 3372–3377.
- [9] M. Halmann, *Nature* 275 (1978) 115–116.
- [10] T. Inoue, A. Fujishima, S. Konishi, K. Honda, *Nature* 277 (1979) 637–638.
- [11] S.C. Yan, S.X. Ouyang, J. Gao, M. Yang, J.Y. Feng, X.X. Fan, L.J. Wan, Z.S. Li, J.H. Ye, Y. Zhou, Z.G. Zou, *Angew. Chem. Int. Ed.* 49 (2010) 6400–6404.
- [12] L. Ye, X. Jin, C. Liu, C. Ding, H. Xie, K.H. Chu, P.K. Wong, *Appl. Catal. B Environ.* 187 (2016) 281–290.
- [13] M. Anpo, H. Yamashita, Y. Ichihashi, S. Ehara, *J. Electroanal. Chem.* 396 (1995) 21–26.
- [14] Z. Xiong, Y. Luo, Y. Zhao, J. Zhang, C. Zheng, J.C.S. Wu, *Phys. Chem. Chem. Phys.* (2016), <http://dx.doi.org/10.1039/c5cp07854g>.
- [15] L. Etgar, W. Zhang, S. Gabriel, S.G. Hickey, M.K. Nazeeruddin, A. Eychmüller, B. Liu, M. Grätzel, *Adv. Mater.* 24 (2012) 2202–2206.
- [16] W.-J. Ong, L.-L. Tan, S.-P. Chai, S.-T. Yong, A.R. Mohamed, *Nanoscale* 6 (2014) 1946–2008.
- [17] B. Li, Z. Zhao, Q. Zhou, B. Meng, X. Meng, J. Qiu, *Chem. Eur. J.* 20 (2014) 14763–14770.
- [18] T.L. Thompson, J.T. Yates, *Chem. Rev.* 106 (2006) 4428–4453.
- [19] S. Liu, J. Yu, M. Jaroniec, *Chem. Mater.* 23 (2011) 4085–4093.
- [20] H.G. Yang, C.H. Sun, S.Z. Qiao, J. Zou, G. Liu, S.C. Smith, H.M. Cheng, G.Q. Lu, *Nature* 453 (2008) 638–642.
- [21] Q. Xiang, K. Lv, J. Yu, *Appl. Catal. B Environ.* 96 (2010) 557–564.
- [22] G. Liu, J.C. Yu, G.Q. Lu, H.-M. Cheng, *Chem. Commun.* 47 (2011) 6763–6783.
- [23] T.R. Gordon, M. Carnello, T. Paik, F. Mangolini, R.T. Weber, P. Fornasiero, C.B. Murray, *J. Am. Chem. Soc.* 134 (2012) 6751–6761.
- [24] Y. Liao, H. Zhang, W. Que, P. Zhong, F. Bai, Z. Zhong, Q. Wen, W. Chen, *ACS Appl. Mater. Interfaces* 5 (2013) 6463–6466.
- [25] W.-J. Ong, L.-L. Tan, S.-P. Chai, S.-T. Yong, A.R. Mohamed, *ChemSusChem* 7 (2014) 690–719.
- [26] B. Zhang, F. Wei, Q. Wu, L. Piao, M. Liu, Z. Jin, *J. Phys. Chem. C* 119 (2015) 6094–6100.
- [27] H.G. Yang, G. Liu, S.Z. Qiao, C.H. Sun, Y.G. Jin, S.C. Smith, J. Zou, H.M. Cheng, G.Q. Lu, *J. Am. Chem. Soc.* 131 (2009) 4078–4083.
- [28] J.S. Chen, Y.L. Tan, C.M. Li, Y.L. Cheah, D. Luan, S. Madhavi, F.Y.C. Boey, L.A. Archer, X.W. Lou, *J. Am. Chem. Soc.* 132 (2010) 6124–6130.
- [29] Z. Zheng, B. Huang, J. Lu, X. Qin, X. Zhang, Y. Dai, *J. Chem. Eur.* (2011) 15032–15038.
- [30] T. Tachikawa, S. Yamashita, T. Majima, *J. Am. Chem. Soc.* 133 (2011) 7197–7204.
- [31] J. Yu, J. Low, W. Xiao, P. Zhou, M. Jaroniec, *J. Am. Chem. Soc.* 136 (2014) 8839–8843.
- [32] D. Zhang, G. Li, X. Yang, J.C. Yu, *Chem. Commun.* 29 (2009) 4381–4383.
- [33] D. Sun, W. Yang, L. Zhou, W. Sun, Q. Li, J.K. Shang, *Appl. Catal. B Environ.* 182 (2016) 85–93.
- [34] J. Yu, Q. Xiang, J. Rana, S. Mann, *CrystEngComm* 12 (2010) 872–879.
- [35] C.K. Nguyen, H.G. Cha, Y.S. Kang, *Cryst. Growth Des.* 11 (2011) 3947–3953.
- [36] X. Li, J. Wang, Y. Men, Z. Bian, *Appl. Catal. B Environ.* 187 (2016) 115–121.
- [37] X. Han, Q. Kuang, M. Jin, Z. Xie, L. Zheng, *J. Am. Chem. Soc.* 131 (2009) 3152–3153.
- [38] L. Ren, Y. Li, J. Hou, J. Bai, M. Mao, M. Zeng, X. Zhao, N. Li, *Appl. Catal. B Environ.* 181 (2016) 625–634.
- [39] X. Zhao, W. Jin, J. Cai, J. Ye, Z. Li, Y. Ma, J. Xie, L. Qi, *Adv. Funct. Mater.* 21 (2011) 3554–3563.
- [40] H. Zhang, Y. Han, X. Liu, P. Liu, H. Yu, S. Zhang, X. Yao, H. Zhao, *Chem. Commun.* 46 (2010) 8395–8397.

- [41] G. Liu, H.G. Yang, X. Wang, L. Cheng, J. Pan, G.Q. Lu, H.-M. Cheng, *J. Am. Chem. Soc.* 131 (2009) 12868–12869.
- [42] J. Yu, G. Dai, Q. Xiang, M. Jaroniec, *J. Mater. Chem.* 21 (2011) 1049–1057.
- [43] G. Liu, C. Sun, S.C. Smith, L. Wang, G.Q. Lu, H.-M. Cheng, *J. Colloid Interface Sci.* 349 (2010) 477–483.
- [44] G. Liu, H.G. Yang, X. Wang, L. Cheng, H. Lu, L. Wang, G.Q. Lu, H.-M. Cheng, *J. Phys. Chem. C* 113 (2009) 21784–21788.
- [45] Y. Wang, C. Feng, M. Zhang, J. Yang, Z. Zhang, *Appl. Catal. B Environ.* 104 (2011) 268–274.
- [46] H. Li, F. Ren, J. Liu, Q. Wang, Q. Li, J. Yang, Y. Wang, *Appl. Catal. B Environ.* 172–173 (2015) 37–45.
- [47] F. Ren, H. Li, Y. Wang, J. Yang, *Appl. Catal. B Environ.* 176–177 (2015) 160–172.
- [48] F. Tian, Y. Zhang, J. Zhang, C. Pan, *J. Phys. Chem. C* 116 (2012) 7515–7519.
- [49] B. Li, Z. Zhao, Q. Zhou, B. Meng, X. Meng, J. Qiu, *Chem. Eur. J.* 20 (2014) 14763–14770.
- [50] Y. Luan, L. Jing, Y. Xie, X. Sun, Y. Feng, H. Fu, *ACS Catal.* 3 (2013) 1378–1385.
- [51] J. Zhu, S. Wang, Z. Bian, S. Xie, C. Cai, J. Wang, H. Yang, H. Li, *CrystEngComm* 12 (2010) 2219–2224.
- [52] T. Tachikawa, N. Wang, S. Yamashita, S.-C. Cui, T. Majima, *Angew. Chem. Int. Ed.* 49 (2010) 8593–8597.
- [53] J. Wang, Z. Bian, J. Zhu, H. Li, *J. Mater. Chem. A* 1 (2013) 1296–1302.
- [54] L. Sun, Z. Zhao, Y. Zhou, L. Liu, *Nanoscale* 4 (2012) 613–620.
- [55] L. Liu, H. Zhao, J.M. Andino, Y. Li, *ACS Catal.* 2 (2012) 1817–1828.
- [56] Q.Y. Zhang, Y. Li, E.A. Ackerman, M. Gajdardziska-Josifovska, H.L. Li, *Appl. Catal. A Environ.* 400 (2011) 195–202.
- [57] Y. Li, W.N. Wang, Z.L. Zhan, M.H. Woo, C.Y. Wu, P. Biswas, *Appl. Catal. B Environ.* 100 (2010) 386–392.
- [58] C.C. Yang, J. Vernimmen, V. Meynen, P. Cool, G.J. Mul, *ACS Catal.* 284 (2011) 1–8.
- [59] Y. Zhao, W. Ma, Y. Li, H. Ji, C. Chen, H. Zhu, J. Zhao, *Angew. Chem. Int. Ed.* 51 (2012) 3188–3192.
- [60] R.E. Rex, F.J. Knorr, J.L. McHale, *J. Phys. Chem. C* 117 (2013) 7949–7951.
- [61] J. Yu, G. Dai, Q. Xiang, M. Jaroniec, *J. Mater. Chem.* 21 (2011) 1049–1057.
- [62] P. Lei, F. Wang, S. Zhang, Y. Ding, J. Zhao, M. Yang, *ACS Appl. Mater. Interfaces* 6 (2014) 2370–2376.